

# The relationship between tectonism and desertification inferred from the provenance and lithofacies changes of the Cenozoic terrestrial sequence of the southwestern Tarim basin

Aki Sakuma (✉ [a.sakuma@eps.s.u-tokyo.ac.jp](mailto:a.sakuma@eps.s.u-tokyo.ac.jp))

Tokyo Daigaku Daigakuin Rigakukei Kenkyuka Rigakubu <https://orcid.org/0000-0002-5228-3730>

Ryuji Tada

Chiba Kogyo Daigaku

Tomohiro Yoshida

Tokyo Daigaku Daigakuin Rigakukei Kenkyuka Rigakubu

Hitoshi Hasegawa

Kochi Daigaku Riko Gakubu Daigakuin Rigaku Senko

Naomi Sugiura

Tokyo Daigaku Daigakuin Rigakukei Kenkyuka Rigakubu

Akinori Karasuda

Tokyo Daigaku Daigakuin Rigakukei Kenkyuka Rigakubu

Ke Wang

Yunnan University

Hongbo Zheng

Yunnan University

---

## Research article

**Keywords:** Tarim basin, Pamir, ESR signal intensity, desertification, Aertashi section, provenance change

**Posted Date:** July 23rd, 2020

**DOI:** <https://doi.org/10.21203/rs.3.rs-44182/v1>

**License:**  This work is licensed under a Creative Commons Attribution 4.0 International License.

[Read Full License](#)

---

**Version of Record:** A version of this preprint was published at Progress in Earth and Planetary Science on August 5th, 2021. See the published version at <https://doi.org/10.1186/s40645-021-00427-6>.

# Abstract

The Tarim basin is one of the most arid areas in the world and its major part is occupied by the Taklimakan desert. Although unraveling the history of aridification of Taklimakan desert is important to understand the global climate change during the Cenozoic, the timing and the mechanism of its formation are still controversial. One of the hypotheses is that the uplift of the Pamir locating to the west of the Tarim basin blocked the intrusion of the moist air and induced the aridification in the Tarim basin. In this study, we explored the linkage between the uplift of the Pamir and the desertification in the Tarim basin during the period from the late Eocene to the middle Miocene. Provenance changes of the fluvial deposits along the Aertashi section, which is located in the southwestern edge of the Tarim basin and offers the longest record with the reliable age model, was examined using Electron Spin Resonance (ESR) signal intensity and crystallinity index (CI) of quartz in the sand fraction of fluvial sandstone and the thin section observation to identify the timings of tectonic events in the Pamir from which clastic materials were supplied by rivers. Our results suggest that major provenance changes in the drainage of the river delivering the clasts to the Aertashi section occurred at ca. 26 Ma, 20 Ma, and 15 Ma. These timings are mostly consistent with the timings observed in the previous provenance studies in the Aertashi section and probably reflect tectonic events in the Pamir. On the other hand, the Tarim basin was under the relatively arid condition after ca. 34 Ma based on the first occurrence of sand dune deposit. Hence, our result does not support the hypothesis that the onset of the aridification in the Tarim basin was caused by the uplift of the Pamir and consequent shut down of the moisture supply from the Paratethys Sea although the afterward intensification of tectonic events in the Pamir might be related to the phased uplift.

## Introduction

The Tarim basin, locating on the north side of the Tibetan Plateau, is one of the most arid places in the world (GPCC, 2018). The major part of the basin is covered by sand dunes that characterize the Taklimakan desert. The wadi and dry lakes locating around the Taklimakan desert are important sources of the aeolian dust and the eliminated dust is considered to have been influencing the Cenozoic climate in the entire northern hemisphere (Uno et al., 2009; Isozaki et al., 2020). Thus, it is essential to reveal the history of the desert. However, when and how the desert was formed is still controversial (Sun et al., 2009; Zheng et al., 2015; Heermance et al. 2018).

Three hypotheses are proposed to explain the Cenozoic aridification of inland Asia and the mechanisms of the formation of the Taklimakan desert. First hypothesis is that the stepwise global cooling throughout the Cenozoic (probably caused by the decrease in the atmospheric  $p\text{CO}_2$ ) affected the regional climate (Dupont-Nivet et al., 2007; Bosboom et al., 2014b). Second hypothesis is that the westward retreat of the Paratethys Sea during the late Eocene decreased the supply of the moisture to the inland Asia, causing aridification there (Ramstein et al., 1997; Bougeouis et al., 2018; Kaya et al., 2019). The last hypothesis is that the uplift of the Tibetan Plateau and the surrounding area of the Tarim basin caused by the collision between the Eurasian continent and the Indian sub-continent blocked intrusion of the moisture supply

from the Paratethys sea and/or the Indian Ocean (Manabe and Broccoli, 1990; Kutzbuch et al., 1993; An et al., 2001; Sun JM et al., 2017; Li et al., 2018; Sun and Liu, 2018). Among mountains surrounding the Tarim basin, the uplift of the Pamir, locating to the west of the Tarim basin, seems especially important for the aridification of the Tarim basin due to its rain shadow effects (Sun and Liu, 2018). The Pamir gained high elevation during the late Cenozoic (Burtman and Molnar, 1993) and this high elevation might have blocked intrusion of the westerly wind to the Tarim basin, leading to the aridification of the basin (Bosboom et al., 2014a; Sun JM et al., 2017). Although these hypotheses have been attempted to be tested, a consensus is yet to be reached (see references above).

One of the reasons for the difficulty in examining the linkage between the aridification in the Tarim basin and the tectonic movement in the Pamir is the large uncertainties of estimated ages of the two events. Ages of the tectonic events in the Pamir have been estimated by several ways, such as the timings of provenance changes in the Cenozoic sequence locating along the southwestern margin of the Tarim basin (e.g. Cao et al., 2014; Blayney et al., 2016), reconstruction of the thermal history of the rocks exposed in the Pamir using thermochronological methods such as biotite and muscovite Ar/Ar dating and zircon and apatite (U-Th-Sm)/He dating (e.g. Sobel and Dumitru, 1997), or the calculation of the subsidence rate from the geological subsurface structure based on seismic reflection data and geological mapping (e.g. Jiang and Li, 2014; Chapman et al., 2017). On the other hand, the timing of the desertification is estimated based on the appearance of the aeolian deposits in the Cenozoic terrestrial sequences of the Tarim basin (Zheng et al., 2006, 2010, 2015; Sun JM et al., 2009; Tada et al., 2010; Sun DH et al., 2011; Sun and Windley, 2015; Heermance et al., 2018). Because the estimated ages of both aridification events of the Tarim basin and tectonic events of the Pamir have errors of several million years, the order of events was yet to be shown. To avoid such a correlation problem, examining the timing of the two events within the same sedimentary sequence is ideal.

Provenance of fluvial deposits, whose drainage includes active tectonic belts such as Pamir, is commonly used to specify the timing of the tectonic events (e.g. Najman, 2006; Cao et al., 2014, 2015). To elucidate the evolution of the Pamir, previous studies reported provenance data such as U-Pb zircon age distributions, detrital apatite fission track and Sm/Nd isotope ratios of sediments from the Cenozoic sequences along the western margin of the Tarim basin (Sobel and Dumitru, 1997; Bershaw et al., 2012; Cao et al., 2014, 2015; Blayney et al., 2016; Clift et al., 2017). Although these studies showed that provenance changes occurred from the late Oligocene to the middle Miocene, exact ages are not well-constrained because of the low sampling resolution due to time-consuming nature of these analyses. Thus, to examine the relationship between the aridification of the Tarim basin and the uplift of the Pamir, it is necessary to investigate the provenance changes in the terrestrial sequences which also preserve the evidence of aridification in the Tarim basin using a new method which enables us the high-resolution analysis.

In this study, we examined the provenance changes in the upper Eocene to lower Miocene fluvial sequence of the Aertashi section located in the southwestern margin of the Tarim basin in order to detect the changes of the drainage area from which we inferred the timings of the tectonic events. We

conducted two types of analyses to investigate the provenance changes of the fluvial sediments supplied by the paleo-Yarkand river in the Aertashi section. The Electron Spin Resonance (ESR) signal intensity and the crystallinity index (CI) of quartz are analyzed for the 64-500  $\mu\text{m}$  fraction of the fluvial sandstone. Generally, quartz is the most abundant mineral in sandstones and resistant to physical and chemical weathering. Also its specific gravity (=density) is close to the bulk sediments. Consequently, it is less influenced by weathering and sorting, and best represents bulk sediments. Thus, it is the ideal material for provenance study. In addition to these measurements, we examined the grain composition of fluvial sandstone by observing thin sections. Finally, we compared the timings of the tectonic events in the Pamir estimated from provenance changes of fluvial sediments with that of the intensified aridification suggested by the occurrence of aeolian deposits to test the linkage between the uplift of the Pamir and the desertification in the Tarim basin.

## Geological Settings

### Location of the studied section and tectonic setting of surrounding areas

The Aertashi section (N37°58', E76°33-34') studied in this research locates in the southwestern margin of the Tarim basin. The Tarim basin locates on the north side of the Tibetan Plateau and surrounded by the Pamir to the west, Kunlun Mountains to the south, Altyn mountains to the southeast, and Tianshan Mountains to the north (Fig. 1a). Cenozoic uplift of these mountains has been considered as associated with the India-Asia collision started at ~50Ma (e.g. Sobel and Dumitru, 1997; DeCelles et al., 2014).

Fluvial sediments deposited along the southwestern margin of the Tarim basin is interpreted to have been supplied dominantly from the Pamir (Zheng et al., 2010; Cao et al., 2015; Blayney et al., 2016). The Pamir terranes are a large arcuate mountain belt and bounded by the Tarim basin on its east with the Kashgar-Yecheng Transfer System (KYTS), by the Tajik basin on its west with the Darvaz fault and by the Alai Valley on its north with the Main Pamir Thrust (Cowgill, 2010) (Fig.1b). The Pamir is divided into four E-W trend terrains by large fault systems in order from north, the North Pamir, the Central Pamir, the South Pamir, and Kohistan-Ladakh terranes, respectively, which were accreted during the late Paleozoic-Mesozoic and each terrain owns specific geological feature (rock types, ages, metamorphic grade, etc.) (Cowgill, 2010; Robinson et al., 2007, 2012). The modern Yarkand river, which runs adjacent to the Aertashi section, drains through the Central and the South Pamirs (Blayney et al., 2016). Although studying the tectonic evolution of the Pamir is important in view of both understanding the process of continental collision and examining its relationship with the climatic change in the surrounding areas, when and how the tectonic events of the Pamir occurred during the Cenozoic is still under debate (Sobel and Dumitru, 1997; Blayney et al., 2016; Cowgill, 2010; Cao et al., 2014; Chen et al., 2018; Wei et al., 2018). Two hypotheses are proposed in previous researches (ex. Sobel and Dumitru, 1997; Blayney et al., 2016; Cowgill, 2010; Cao et al., 2014; Chen et al., 2018; Wei et al., 2018). The first hypothesis is that the Pamir salient lay in line with Kunlun Mountains before Oligocene and started to move northward for ~300 km

since ~25 Ma (Cowgill, 2010; Sobel et al., 2013; Blayney et al., 2016). This displacement is presumed as a result of the onset of the KYTS dextral movement (Cowgill, 2010; Cao et al., 2014; Blayney et al., 2016) and the southward subducted slab under the Pamir is attributed to the northward movement of the Pamir (Burman and Molnar, 1993). The rapid exhumation in the Pamir salient initiated during the late Oligocene~early Miocene according to the thermochronological dating suggests the large-scale uplift at that time caused by N-S shortening (e.g. Sobel and Dumitru, 1997; Robinson et al., 2007; Amidon and Hynek, 2010). The other hypothesis suggests that there existed antecedent Pamir before Cenozoic and its displacement relative to the Tarim during the Cenozoic is only tens of kilometers (Chen et al., 2018; Wei et al., 2018). The deposition of the alluvial conglomerates along the edge of the Pamir also occurred during the Paleogene and it is unlikely that these coarse sediments deposited away from the mountain ranges of the Pamir, suggesting the limited amount of the displacement of the Pamir during the Neogene (e.g. Chen et al., 2018). Thermochronological dating of sedimentary rocks distributing in the western margin of the Tarim basin and metamorphic rocks in the Pamir also shows Paleogene ages in addition to Oligocene to Miocene ages, which indicates the intensification of exhumation in the Pamir occurred before the Neogene (e.g. Cao et al., 2015; Rutte et al., 2017).

## Stratigraphy of the Aertashi section

The Cenozoic sedimentary sequence of the Aertashi section is composed of four formations and one group, which are the Wulagen Formation, the Bashibulake Formation, the Wuqia Group, the Artux Formation and the Xiyu Formation in ascending order (Zheng et al., 2015) (Fig. 2). The lithology of each formation is briefly summarized below based on the field observation of this study and description of previous studies (Zheng et al., 2010, 2015; Bosboom et al., 2011, 2014; Blayney et al., 2016, 2019; Wei et al., 2018).

The Wulagen Formation mainly consists of green mudstone intercalated with greenish grey limestone rich in bivalve fossils and green fine sandstone, and is ca. 80 m thick in the studied section (Bosboom et al., 2011, 2014). The depositional environment of this formation is interpreted as the nearshore to shallow marine based on the fossil assemblages of bivalves, ostracods, calcareous nannofossils and foraminifera (Bosboom et al., 2011, 2014).

The Bashibulake Formation conformably overlies the Wulagen Formation with sharp contact and the boundary is easily recognized by the change of color (Bosboom et al., 2011). The formation is characterized by alternations of the decimeter thick, dominantly reddish brown mudstone and red fine sandstone. In the lower unit of this formation, red fine sandstone often shows parallel laminations or trough cross laminations, which disappears upwards. The desiccation cracks appear at the top of the mudstone layers and chicken wire gypsums are found within mudstone in the middle unit of the formation. The upper unit of the formation dominantly comprises paleosol mudstone and red fine sandstone showing reverse grading. The thickness of this formation is ca. 850 m. The depositional

environment is interpreted to have been changed from the nearshore lakes or playa to the flood plain (Blayney et al., 2019; Zheng et al., 2010, 2015).

The Wuqia Group overlies the Bashibulake Formation unconformably (Zheng et al., 2015; Blayney et al., 2016, 2019) and is divided into three units characterized by alteration of red sandstone and reddish brown mudstone. The lower unit of this group comprises 0.8 to 1 m thick well-sorted red fine sandstone beds, showing high angle trough cross bedding, with rare reddish brown mudstone intercalations. Sandstone with large-scale cross beds of the lower unit are interpreted as the sand dune deposit (Zheng et al., 2010; Blayney et al., 2019). The thickness of the lower unit is ca. 150 m. The middle unit is composed of red fine sandstone intercalated with reddish orange fine sandstone and brown mudstone. Reddish orange fine sandstone shows an erosional contact at its base, suggesting reddish orange fine sandstone was formed under river stream. The thickness of the middle unit is ca. 400 m. The upper unit mainly consists of red fine sandstone and brown mudstone that are occasionally intercalated with yellow siltstone and gray fine sandstone with cross lamina. The sandstone beds show thickening upward trend through the upper unit. The thickness of the upper unit is ca. 550 m. The sedimentary environment of the middle and upper units is interpreted as meandering river system (Zheng et al., 2010, 2015; Blayney et al., 2019). The total thickness of the group is ca. 1100 m.

The Artux Formation conformably overlies the Wuqia Group, whose base is defined as the first appearance of pebble conglomerate. The formation is dominated by the alteration of pink, orange, and yellow sandstone and red, reddish brown, and brown mudstone with pebble conglomerate intercalations. The formation is divided into two units based on their lithology. The base of the lower unit is defined by the first appearance of the granule to pebble conglomerate bed which contains large limestone clasts up to 0.5 m in diameter (Zheng et al., 2010, 2015; Blayney et al., 2019). The lower unit is composed of pinkish fine sandstone interbedded with granular to pebble conglomerate and mudstone. Matrix-supported conglomerate occasionally show reverse grading which is the typical feature of the debris flow deposits in the alluvial fan. In addition, granule lenses and cross beddings are found within sandstone layers. These features suggest this unit is distal fan deposit (Zheng et al., 2010; Blayney et al., 2019). The thickness of the lower unit is ca. 700 m. The upper unit is characterized by alteration of orange to yellow fine sandstone with ripple marks and reddish brown mudstone with rare intercalation of granule layers. Granule layers occasionally erode the underlying layers in the upper part of the upper unit. The channels filled by trough cross-bedded sands with some floating pebbles are observed in this unit (Blayney et al., 2019). The depositional environment is interpreted as a distal alluvial fan with abundant crevasse and flood deposit (Zheng et al., 2010; Blayney et al., 2019). The thickness of the upper unit is ca. 1050 m. The total thickness of this formation is ca. 1750 m.

The Xiyu Formation overlies the Artux Formation with a sharp contact. The Xiyu Formation is dominated by dark grey conglomerate, consisting of poorly-sorted, well-rounded pebbles to boulders including basement rocks and volcanic rocks with clast-supported fabric and rare medium sandstone intercalations with cross bedding (Blayney et al., 2019). The depositional environment of this formation is interpreted as the middle to proximal alluvial fan based on the appearance of conglomerate described above (Zheng et

al., 2010, 2015; Blayney et al., 2019; Wei et al., 2018). The thickness of this formation is more than 5000 m.

## Age model

Three types of the data are available to constrain the age model of the Aertashi section; biostratigraphy, U-Pb zircon chronology of volcanic material, and magnetostratigraphy (Yin et al., 2002; Bosboom et al., 2011, 2014; Zheng et al., 2015; Wei et al., 2018). Bosboom et al. (2011, 2014) estimated the age of the Wulagen Formation at several sections in the western Tarim basin to specify the timing of the retreat of the Paratethys Sea. They identified foraminifera, ostracods, bivalves, calcareous nannofossils and dinoflagellate cysts in the Wulagen Formation and concluded that the formation belongs to Zone CP14 (GTS2012) of calcareous nannofossil zonation based on calcareous nannofossils and dinocysts assemblages (Bosboom et al., 2011, 2014). Zheng et al. (2015) carried out the dating of the ash layer from the upper part of the Xiyu Formation using dating of biotite grains and U-Pb dating of zircon grains and concluded that the eruption occurred around 11 Ma and supplied the ash instantaneously to the Aertashi section. Bosboom et al. (2014b), Zheng et al. (2015), and Blayney et al. (2019) conducted the magnetostratigraphic studies at the Aertashi section and constructed magnetostratigraphy-based age models independently. All of these studies show very similar age models. However, the sampling routes of Bosboom et al. (2014b) and Blayney et al. (2019) are partly different from the route of this study while that of Zheng et al. (2015) is exactly the same. Thus, in this study, we adopted the age model of Zheng et al. (2015).

## Samples And Methods

### Samples for the analyses

Approximately 200g of sandstone samples were collected throughout the Aertashi section at stratigraphic intervals of ~50 m during the field surveys in 2007 and 2010. In order to reconstruct the river drainage evolution and tectonic impact on it by examining provenance changes of fluvial deposits, 59 fluvial fine sandstone samples were selected for the ESR and CI analyses and 27 sandstone and conglomerate samples were selected for thin section observation, respectively. These samples cover the entire sequence from the base of the Bashibulake Formation to the base of the Xiyu Formation. The sampling location and stratigraphic position of each sample are shown in supplementary table 1.

### Pre-treatment of the samples for the ESR and CI analysis

Prior to the ESR and CI analyses, carbonate, iron and manganese oxides, and organic matter were removed from the samples by chemical treatments (Tada et al., 2000). Approximately two grams of disaggregated samples were acidified with 40 ml of 20 vol. % acetic acid solution at 40°C for 2 hours to remove carbonate. To remove iron and manganese oxides, the samples were treated with 40 ml of 0.3 M

sodium citrate solution, 5 ml of 1.0 M sodium bicarbonate solution and 1.5 grams of sodium dithionite at 80°C. Organic matter was removed with 40 ml of 10 vol. % hydrogen peroxide solution at 60°C for 10 hours.

The grain size distributions were measured for all the samples analyzed for the ESR and CI to identify the fraction used for the analyses. The grain size measurement was conducted at room temperature using a laser diffraction particle size analyzer (Malvern, Mastersizer 2000) at the University of Tokyo. Approximately 50 mg of homogeneous aliquot of each pre-treated sample was emptied into the analyzer filled with deionized water and circulated in closed transport circuit. To disperse the particles, the sample was ultrasonicated for 5 min before the measurement and stirred at 2000 rpm throughout the measurement. The measurement was repeated five times in a row and the result was averaged for each sample. The measurement was conducted for the diameter range between 0.02 to 2000  $\mu\text{m}$ . The reproducibility was better than  $\pm 1.0 \mu\text{m}$  for the median diameter in five times measurements of the replicated standard sample of soda lime glass beads (UB-911L, UNITIKA Ltd.).

All of the fluvial sandstone samples showed multimodal grain size distributions. Selected representative samples are shown in Fig. 3 and all data are shown in supplementary table 2. In general, multimodal distribution is composed of several log-normal distributions, each of which is considered as representing the set of particles transported by different mechanisms such as suspension, saltation and bottom traction (e.g. Sun et al., 2002). Thus, numerical partitioning into the subcomponents was conducted using the solution tool of MS Excel following the method of Sun et al. (2002). All of our samples show three modes. The median diameter of these three subpopulations range from 1.7-12.5  $\mu\text{m}$ , 6.5-80.1  $\mu\text{m}$  and 40.1-300  $\mu\text{m}$  and the averages are 5.1  $\mu\text{m}$ , 26.6  $\mu\text{m}$  and 106  $\mu\text{m}$ , respectively. The coarsest fraction which roughly correspond to 64-500  $\mu\text{m}$  (fine to medium sand) fraction is coarser than the subpopulation representing the eolian dust and is considered as representing particles transported by bottom traction in the river and derived from the host rocks exposed in the drainage area (Isozaki, 2020). In this study, this fraction was extracted from a bulk sample by sieving and used for the ESR and CI analyses.

## The ESR and CI analyses

The number of lattice defects with unpaired electrons of minerals can be evaluated by the ESR signal intensity of the  $E_1'$  center of quartz (Toyoda, 1992). The  $E_1'$  center of quartz is an unpaired electron in single silicon  $sp^3$  orbit oriented along a bond direction into an oxygen vacancy (Feigl et al., 1974) and used to estimate the amount of oxygen vacancies in quartz, which increases with the age of quartz grains (Toyoda and Hattori, 2000). Namely, high value of the ESR signal intensity of quartz suggests that quartz grains were supplied from old host rocks. To measure the ESR signal intensity of quartz, first, the 64-500  $\mu\text{m}$  fractions of pretreated samples were irradiated with gamma ray (total dose of 2.5kGy) using a  $^{60}\text{Co}$  source at Takasaki Advanced Radiation Research Institute, National Institutes for Quantum and Radiological Science and Technology to create hole centers. Then, approximately 0.1 gram of irradiated samples are heated at 300°C for 15 minutes to convert the oxygen vacancies to  $E_1'$  center. The ESR signal

intensity was measured at room temperature with X-band ESR spectrometer (JEOL, JES-FA100) at the University of Tokyo under 0.01 mW of microwave power, 0.1mT magnetic field modulation (100kHz), 5mT scan range, 2 minutes scan time, and 0.03 second time constant. The ESR signal intensity is expressed in spin units (1 spin unit = spins/g) (Toyoda and Naruse, 2002).

The quartz content (QC) was measured by the internal standard method (Klug and Alexander, 1974) with silicon powder (Wako Pure Chemical Industries, Ltd.) as an internal standard, using PANalytical X'Pert PRO X-ray diffractometer (XRD) at the University of Tokyo with Cu target. The measurement condition was set as the tube voltage of 45kV, the tube current of 40 mA, the slit of 1°, scanning interval of 20 to 30 °2θ, the time per step(s) of 6.35, and scan speed of 0.334 °/s. The error of the quartz content estimation was better than ±8.5 wt%.

The Crystallinity Index (CI) of quartz defined by Murata and Norman (1976) was calculated from the X-ray diffraction data. The CI measurement was also conducted using the same XRD. The measurement condition was set as the tube voltage of 45kV, the tube current of 40mA, the slit of 1°, scanning interval of 65 to 75 °2θ, the time per step(s) of 22.86, and scan speed of 0.02321 °/s. The error of the CI for the three repeated measurements is better than ±0.25.

## Observation of thin sections

Thin section observation of fluvial sandstone and conglomerate in Aertashi section was conducted in order to estimate the rock types exposed in the source area. Thirty-eight samples are impregnated with epoxy resin Devcon ET-300 and Petropoxy 154 and thin sections of impregnated samples were made. Seven samples selected to cover the entire sequence were point-counted at a step of 0.5 mm. At least 500 points excluding matrix and pore were counted for every sample.

## Results

### Results of the ESR signal intensity and the CI analyses

The temporal change of the ESR signal intensity of quartz in the 64-500 μm fraction is shown in Fig. 4. The ESR signal intensity ranges from 4.0 to 18.7, with the average of 10.9 and the standard deviation of 3.4, respectively. The ESR signal intensity fluctuates between 5.4 and 11.8 from 0 m level at the base of the Bashibulake Fm. to 1500 m level in the middle part of the Wuqia Gr. At the level of 1500 m which coincides with the first appearance of yellow siltstone, the ESR signal intensity abruptly increases to 15.6. The ESR signal intensity ranges between 13.0 and 18.7 from 1500 m to 2200 m level in the lower part of the Artux Fm. Between the levels of 2200 m and 3000 m in the middle part of the Artux Fm., the ESR signal intensity fluctuates significantly between 7.4 and 18.5. Between the levels of 3000 m and 3600 m in the upper part of the Artux Fm., the ESR signal intensity becomes lower again and fluctuates with smaller amplitude between 9.0 and 12.6. At 3600 m level at the base of the Xiyu Fm., the ESR signal intensity suddenly decreases to 4.0.

The temporal change of the CI of quartz in the 64-500  $\mu\text{m}$  fraction is shown in Fig. 4. The CI ranges between 7.15 and 8.44 with the average of 8.05 and the standard deviation of 0.27. The CI shows low value between 7.15 and 8.06 from the level of 0 m to 800 m in the Bashibulake Fm. From the boundary between the Bashibulake Fm. and the Wuqia Gr. at 800 m level, the CI starts to increase gradually up to the level of 1500 m at which the CI reaches approximately 8.2. Above the level of 1500 m, the CI fluctuates between 7.98 and 8.44.

## Thin section observation

Before the point counting, grain components such as detrital minerals and lithic fragments in samples were identified from 38 thin sections in order to estimate the rock types exposed in source areas and are described below. Grain composition described below is as per total grains.

Quartz is the most dominant mineral in all the samples examined. Three types of quartz grains are identified: monocrystalline, polycrystalline and chalcedonic. Monocrystalline quartz is the most dominant type of quartz in all the samples examined with the maximum of 61.9%, minimum of 24.9% and the average of 51.0% and accounts for more than two thirds of quartz grains. About a half of monocrystalline quartz grains show wavy extinction. Polycrystalline quartz is also commonly found in studied samples with the maximum of 10.3%, minimum of 3.6% and the average of 6.0%. It shows unclear crystal boundary and various sizes of crystals are included from silt size to coarse sand size. Colorless chalcedonic quartz without impurities is rarely found.

Feldspar is the second dominant detrital mineral and account for relatively small percentage with the maximum of 17.8%, minimum of 6.8%, and the average of 11.6%. Three types of feldspar grains are identified: orthoclase, plagioclase and microcline. Among feldspar grains, orthoclase grains are far more abundant (average 10.3%) than plagioclase (average 0.8%) and microcline (average 0.5%) grains although their relative ratio varies slightly among samples.

Accessory detrital minerals such as micas, mafic minerals, and opaque minerals, are identified with minor amounts (average 3.4%). Biotite is the most common accessory detrital mineral and is especially abundant in the Xiyu Fm. Biotite grains observed in the Xiyu Fm. are relatively large ( $\sim 500 \mu\text{m}$ ) and mostly have pleochroism exhibiting brown~green color under open nicol. Other accessory detrital mineral grains are silt size and weathered, which makes them hard to be identified.

Lithic fragments are classified into six groups: (1) limestone lithics, (2) mudstone lithics, (3) sandstone lithics, (4) chert lithics, (5) volcanic lithics, and (6) metamorphic lithics (Fig. 5). Plutonic lithic fragment is not observed in thin sections possibly because the grain size of samples is finer than the size of crystals in plutonic rocks.

Limestone lithics account for 1.3-17.0% with the average of 7.5%. Limestone lithic mostly consists of micritic calcite with some detrital quartz grains (Fig. 5a). Ghost of fossils such as foraminifera are

occasionally observed in limestone lithic. The limestone lithic fragments are indented by other clastic grains and show concave contacts due to pressure dissolution.

Mudstone lithics account for 0.7-17.6% with the average 6.3%. Four types of mudstone lithic fragments are found. Siltstone lithic is composed of silt-size grains of quartz and feldspar with small amount of the matrix that is composed of clay minerals, iron oxides and other clay size particles (Fig. 6a). Siliceous siltstone lithic is composed of silt size quartz grains with microcrystalline quartz cement (Fig. 6b). The sorting of siliceous siltstone is good. Claystone lithic consists mostly of clay minerals, iron oxides and other minerals with rare silt-size quartz grains (Fig. 6c). Siliceous claystone lithic is mostly composed of detrital quartz grains cemented with silica of microcrystalline quartz with minor iron oxides and opaque minerals (Fig. 6d).

Sandstone lithics are accounted for 0~4.8% with the average of 1.4%. Some samples do not contain sandstone lithics because of their smaller grain sizes. Four types of sandstone lithic fragments are identified. Quartzo-feldspathic sandstone lithic is composed dominantly of quartz with minor feldspar (Fig. 6e). It is poorly sorted but matrix is rare. Ortho-quartzite lithic is composed of well-sorted and rounded single crystal quartz grains (Fig. 6f). Calcite cement is slightly observed and no porosity exists. The grain contacts are generally concave-convex and sutured. Siliceous sandstone lithics are composed mostly of quartz grains with minor lithic fragments and feldspar. It contains ~30% of microcrystalline quartz cement. Siliceous sandstone lithic is often suffering from weathering, showing secondary minerals. Quartz wacke lithic consists of quartz grains with abundant (~50%) matrix of clay minerals and other minute particles (Fig. 5b).

Chert lithic is less common compared to other sedimentary rock lithics and its content ranges from 0.9% to 5.2% with the average of 2.4%. It consists of microcrystalline quartz cement by more than 95 percent with rare clay-size particles of other detrital minerals such as clay minerals and opaque minerals (Fig. 5c). Quartz crystals are less than 64  $\mu\text{m}$  size and the grain boundary seems irregular although it is not clear due to small crystal size.

Volcanic lithics are rare (less than 3%) and found mostly from the Xiyu Fm. It mainly contains a few tabular or needle shape euhedral phenocrysts in opaque groundmass (Fig. 5d). Blayney et al. (2016) reported that sandstones of the Aertashi section from the Wuqia Gr. to the Artux Fm. contain more than 50% of volcanic fragments. However, their observation is not consistent with our observation that volcanic fragments are rarely found in samples taken from the Bashiblake Fm. To the Artux Fm. Types of gravels in conglomerate of the Artux Fm. are dominantly composed of limestone and sandstone with minor igneous and metamorphic rocks (Blayney et al., 2019). Thus, it is unlikely that only sandstone samples contain large amounts of volcanic rock fragments.

Metamorphic lithics include schist and meta-quartzite. Meta-quartzite lithic (average 5.2%) is more abundant than schist lithic (average 0.3%) (Fig. 5e). Schist lithics include quartz schist, pelitic schist, and psammitic schist lithics (Fig. 5f). Some of meta-quartzite lithics are equigranular and straight grain

boundary while others consist of various size of quartz grains and show unclear and wavy boundary, which are likely to be recrystallized.

Authigenic minerals occur mostly as cement filling intergranular space, and include calcite, iron oxides and silica. Sparry calcite cement is most abundant and iron oxide cement is the second abundant.

## **Temporal changes in the grain composition of sandstone**

The temporal changes in the grain composition based on the point counting result is shown in Fig. 7b. All the samples have less than 15 % of matrix and are classified as lithic arenite which is consistent with the previous study of Blayney et al. (2016) (Fig.7a). To identify the change in types of source rocks, the Q-F-L plot is shown in Fig. 7a and the change in lithic composition is shown in Fig. 7b.

Sandstone samples from the Bashibulake Fm. to the Artux Fm. show relatively similar grain composition. They dominantly consist of monocrystalline quartz with minor feldspar, lithic fragments and rare accessory minerals. Common types of lithic fragments are siliciclastic rocks, limestone, chert and metamorphic rocks. Only one sample from the Artux Fm. (AT07-52cgl) contains a small amount of volcanic rock fragments. Two samples from the lower part of the Wuqia Gr. (AT10-21 and AT10-24) show high percentage of limestone fragments of more than 10 %. The sample from the lower part of the Artux Fm. (AT07-52cgl) contains larger amount of sandstone fragments, which could be due to the larger grain size of the sandstone. The sample from the upper part of the Artux Fm. (AT07-61) contains relatively high amounts of accessory minerals (5.7 %), especially opaque minerals (3.6 %), which is more than twice as large as those of other samples from the strata below the Artux Fm. On the other hand, the sample from the Xiyu Fm. (AT10-49a) show distinctly different composition compared to samples from other formations. It contains less detrital quartz (24.9 %) and more lithic fragments (54.8 %) that include 5.0 % of volcanic lithic. Moreover, the percentage of accessory minerals (11.8 %) is more than twice larger than that of other samples.

## **Discussion**

### **Stage division of the provenance changes and source of coarse detrital materials in fluvial sandstone**

Based on the result of the ESR and CI analyses of the 64-500 $\mu$ m fraction of fluvial sandstone in the Aertashi section, temporal variation in provenance is divided into 6 stages from stage 1 to 6 in the ascending order (Fig. 4). To demonstrate the difference between stages, a diagram that shows the ESR signal intensity vs the CI relationship is made (Fig. 8). The feature of changes in the ESR signal intensity and the CI of each stage is described and the provenance of coarse detrital materials of each stage is discussed below based on the ESR signal intensity, the CI, and the composition of fluvial sandstone.

Stage 1 (ca. 39-34Ma) corresponds to the Bashibulake Fm. whose stratigraphic interval ranges from 0 m to 800 m level. In stage 1, the ESR signal intensity shows relatively low value ranging from 5.4 to 11.2 with the average of 8.5 and standard deviation of 1.8, and the CI shows low values ranging from 7.15 to 8.06 with the average of 7.74 and standard deviation of 0.26. In stage 1, relatively large variations of the ESR signal intensity and the CI support that the provenance is multiple sources. Considering the rapid change of sedimentary environment Fm. from a lagoon, a playa lake, and then floodplain through the Bashibulake (Zheng et al., 2010), the site was not under the influence of a single river system but clasts might be occasionally transported along shore by the coastal currents during this interval. The grain composition of fluvial sandstone suggests that fragments of sandstone, mudstone, limestone, chert and metamorphic rocks are supplied from its drainage. On the other hand, there is no igneous rock fragment observed. The ESR signal intensity of quartz between 5.4 and 11.2 suggests the source rocks are probably Paleozoic in age whereas the U-Pb age of zircon grains contained in fluvial sandstone ranges from Jurassic to Archean (Blayney et al., 2016). No modern river sediments in the eastern part of the Pamir show zircon age peaks around 1.9 Ga and 300 Ma that are observed for samples taken from the Bashibulake Fm. (Blayney et al., 2016), suggesting at least some of detrital grains in the Bashibulake Fm. were supplied from rocks that are not exposed in the modern drainage areas of the rivers in the eastern Pamir. Moreover, the lack of volcanic lithic fragments suggests volcanic rocks are not exposed in the catchment area and the river head didn't reach the exposure of Triassic volcanic rocks in the North Pamir terrane. Thus, the basin infill of Mesozoic~Paleozoic sandstone, mudstone and limestone exposing along the western edge of the Tarim basin are likely the source of the fluvial sediment in the Aertashi section.

Stage 2 (ca. 34-26 Ma) corresponds to the lower to middle part of the Wuqia Gr. That is from 800 to 1500 m in stratigraphic level. The boundary between stage 1 and stage 2 is defined by the initiation of the long-term gradual increase in the CI, which coincides with the boundary between the Bashibulake Fm. and the Wuqia Gr. In Stage 2, the ESR signal intensity keeps low values ranging from 6.7 to 11.8 with the average of 9.5 and standard deviation of 1.5 while the CI gradually increases from 7.83 to 8.26 with the average of 8.02 and standard deviation of 0.13. The gradual increase of the CI in stage 2 suggests that the increase in relative contribution of more crystallized quartz. On the other hand, the low and stable values of the ESR signal intensity and the clasts composition similar to stage 1 suggest that the provenance did not change significantly from stage 1 to stage 2. These observations imply that the drainage area did not change significantly but the river gradually eroded into deeper level and started to supply more crystallized rocks.

Stage 3 (ca. 26-20 Ma) corresponds to the upper part of the Wuqia Gr. and the lower part of the Artux Fm. that ranges from 1500 m to 2200 m in stratigraphic level. The boundary between stage 2 and stage 3 is marked by the abrupt increase in the ESR signal intensity at ca. 1500m, which coincides with the first appearance of the yellow siltstone. In Stage 3, the ESR signal intensity shows high value ranging from 13.0 to 18.7 with the average of 15.5 and standard deviation of 1.9, while the CI increase stops and has relatively high and stable values between 8.04 and 8.39 with the average value of 8.25 and standard deviation of 0.11. The abrupt increase in the ESR signal intensity and the relatively high CI suggest the increase in contribution of source rocks which contain older quartz grains at the base of stage 3. Lithic

composition suggests host rock types did not change significantly from stage 2 to stage 3 but weakly metamorphosed rocks such as meta-quartzite and polycrystalline quartz, siliciclastic sedimentary rocks, and limestone became dominant while igneous rocks and highly metamorphosed rocks were nearly absent in the source area. According to Blayney et al. (2019), Sm-Nd isotope values of mudstone also shows the sudden negative shift around the base of stage 3, indicating the appearance of the more crustal source rocks. In the North Pamir terrane, Paleozoic (meta)sedimentary rocks are exposed (Cowgill, 2010) and this is likely the source of rocks containing older quartz grains with high ESR signal intensity characteristic of stage 3. While the ESR signal intensity changed considerably between stage 2 and stage 3, the types of lithic fragments, the CI and the zircon age distribution did not change significantly (Blayney et al., 2016), although the contribution of each rock type changed.

Stage 4 (ca. 20-17 Ma) corresponds to the middle part of the Artux Fm. from 2200 m to 3000 m in stratigraphic level. From the boundary between stage 3 and stage 4, the ESR signal intensity starts to oscillate with large amplitude, which ranges between 7.4 and 18.5 with the average value of 12.4 and standard deviation of 4.5, while the CI keeps stable value ranging from 8.04 to 8.41 with the average value of 8.23 and standard deviation of 0.14. The ESR signal intensity vs the CI plots fall into two groups, one is similar to those of stage 3 and the other is similar to those of stage 5. Oscillations of the ESR signal intensity in stage 4 are interpreted as reflecting switches in provenance between two distinctly different sources during this period.

Stage 5 (ca. 17-15 Ma) corresponds to the upper part of the Artux Fm. from 3000 m to 3600 m in stratigraphic level. The boundary between stage 4 and stage 5 is defined by the start of the stable values of the ESR signal intensity. In stage 5, the ESR signal intensity keeps stable and moderate values ranging from 9.0 to 12.6 with the average value of 11.5 and standard deviation of 1.1, and the CI also keeps stable high values ranging from 8.01 to 8.44 with the average value of 8.23 and standard deviation of 0.14. The stable moderate ESR signal intensity and the stable high CI suggest the provenance is stable and correspond to one of the two sources in stage 4. In stage 5, the accessory minerals such as biotite and mafic minerals increases compared to earlier stages and the schist fragments started to appear for the first time in the studied sequence, indicating the appearance of igneous and metamorphic source rocks containing more accessory minerals. This in turn implies the acquisition of the new drainage in the North Pamir where these rocks exposes (Cowgill, 2010). However, assemblages of other grains and lithic fragments are not changed significantly, suggesting the main source area is similar to that of the earlier stages.

Stage 6 (ca. <15 Ma) corresponds to the lower part of the Xiyu Fm. above 3600 m in stratigraphic level. At the boundary between stage 5 and stage 6, the abrupt decrease in the ESR signal intensity occurs. In stage 6, the ESR signal intensity shows very low value of 4.0 while the CI is 7.98 which is similar to the values in the underlying stage 5. In stage 6, the ESR signal intensity and the grain composition indicate that the source rocks of fluvial sediments changed drastically from stage 5. The low ESR signal intensity value suggests that average age of quartz grains in source rocks became younger, probably Mesozoic. According to the thin section observation, the grain composition of the fluvial sandstone of the Xiyu Fm.

changes significantly from the Artux Fm., showing wider variety of lithic fragments such as volcanics and schists, in addition to sandstones, limestones and minor weakly metamorphosed rocks in the Artux Fm., suggesting drainage further expanded into the Pamir and acquired additional types of host rocks including volcanic rocks and schists. Moreover, the percentage of biotite increases abruptly at the base of stage 6, which indicates the detrital supply of acidic igneous rock fragments that contain large biotite crystals started from stage 6. Acidic igneous rocks are not exposed in the area to the east of the KYTS. Therefore, it is expected that the river drainage reached the area near Kongur Shan Fault where Mesozoic igneous rock exposes. This is consistent with the observation that the zircon age distribution pattern of sandstone in stage 6 shows distinctive peaks of early Mesozoic which are attributed to the North Pamir terrane based on the resemblance to those in the modern river sediments supplied from the North Pamir terrane (Blayney et al., 2016; Wei et al., 2018).

## Cause of the provenance changes

The transition from stage 1 to stage 2 at ca. 34 Ma is marked by a relatively small change in the CI and caused by the appearance of the steady river system as we discussed before. Since the drainage area did not change significantly as is suggested by little change in the ESR signal intensity, grain composition, and the age distribution of zircon grains (Blayney et al., 2016), it is unlikely that a significant tectonic movement occurred in the drainage of the paleo-Yarkand river at the boundary between stages 1 and 2. The initiation of the increase in the CI at the base of stage 2 might be attributed to gradual unroofing and consequent increase in supply of more crystallized rocks. It is reported that deformation of the metamorphic dome in the Central and the South Pamir started since the Eocene and the metamorphism prograded northward during late Eocene to Oligocene (Smit et al. 2014; Sterns et al., 2015). On the other hand, the changes in climate and vegetation are reported around 34 Ma all over the world (Dupont-Nivet et al., 2007; Hoorn et al., 2012; Huang and Hinnov, 2019) and such a significant environmental change might have been related to the change of the drainage area. Because there are few studies about the climatic change in the Pamir during Eocene-Oligocene transition, we cannot exclude the possibility of climatic change as the cause of intensified erosion at this moment although it is less likely.

At the boundary between stage 2 and stage 3 (ca. 26 Ma), the host rock which contains older quartz grains of meta-sedimentary rock origin derived from the east part of the North Pamir terrane suddenly appeared, suggesting that the paleo-Yarkand river acquire the new source in a short period. There are two possibilities for the river to supply fragments of older source rocks. One is the river acquired a new drainage area upstream where older meta-sedimentary rocks are exposed. The other is the underlying older strata were newly exposed in the drainage area due to the uplift and rapid erosion within the same drainage area. The latter possibility is less plausible because the strata in the eastern part of the Pamir is relatively thick and the dip angle is nearly vertical (Cowgill, 2010). Therefore, we prefer the first possibility that the river head of the paleo-Yarkand river extended into the North Pamir terrane and the river acquired the new drainage at the beginning of stage 3. This is likely to be caused by the uplift of the eastern North Pamir terrane. In the surrounding areas of the Pamir, evidence for the tectonic events was examined using

other methods such as geothermometer and seismic refraction, which suggest the tectonic activity near the Pamir during late Oligocene to early Miocene (e.g. Sobel et al., 2013; Jiang and Li, 2014). In the north Pamir, the exhumation rate was accelerated during early Miocene which is suggested by the thermal modeling based on the (U-Th)/ He dating of zircon and apatite (Amidon and Hynek, 2010). In the Tian Shan Mountains locating to the north of the Pamir, the rapid exhumation event is suggested based on apatite fission track data, which is interpreted as due to the activation of the Talas-Fergana faults, one of the largest faults in the area, and N-S trend shortening occurred in the area surrounding the Pamir at ca. 25 Ma (Bande et al., 2015).

In stage 4, onset of the fluctuation of provenance between two sources suggests expansion of the drainage area occurred in the upper stream of the paleo-Yarkand river that started to provide clastics of younger ages at ca. 20 Ma. The first conglomerate appeared at the bottom of the Artux Fm. (= middle part of stage 3) and this is interpreted to imply the change in depositional environment to more proximal to the mountains (Zheng et al., 2010), indicating the start of tectonic activity such as the initiation of the fault movement in the eastern Pamir around ca. 20 Ma. In fact, Sobel and Dumitru (1997) dated the clasts of fluvial sediment along the piedmont of the Western Kunlun Shan by apatite fission track and found out cooling ages are roughly 20 Ma, which is interpreted to be associated with the KYTS.

The steady river course was established at ca. 17Ma judging from the stable values of the ESR signal intensity and the CI in stage 5. Stage 5 is interpreted to have been the interval of less intense tectonic activity.

The largest change of the drainage occurred at the boundary between stage 5 and stage 6 (ca. 15 Ma), which is characterized by the significant change of the ESR signal intensity, grain composition, and lithology as well as U-Pb age distribution of zircon grains (Blayney et al., 2016). Deposition of the thick pebble conglomerate of the Xiyu Fm. suggests that the Aertashi section was located in the middle of the alluvial fan and the mountain range of the Pamir came closer to the section. This, in turn, strongly suggests that the deposition of the Xiyu Fm. started when the uplift of the North Pamir terrane occurred (e.g. Blayney et al., 2016; Wei et al., 2017; Zheng et al., 2006). Acquisition of the new source is expected to be caused by this tectonic change.

## **Relationship between the uplift of the Pamir and the aridification in the Tarim basin**

In previous studies, the timing of aridification in the Tarim basin is estimated based on the first appearance of the sand dune or loess deposit in the Cenozoic sequence (Sun et al. 2009; Zheng et al., 2015; Heermance et al., 2018). In the Aertashi section, the deposition of the sand dune sediments started from the bottom of the Wuqia Gr. at ca. 34 Ma (Blayney et al., 2019), indicating relatively dry condition with poor vegetation. On the other hand, the result of this study suggests that the provenance of fluvial sediments did not change significantly during stages 1 and 2 (ca. 39-26 Ma), suggesting significant

tectonic event that affected the drainage of the paleo-Yarkand river did not occur in the Pamir in association with the aridification in the Tarim basin. In other words, the initial aridification in the Tarim basin occurred before the significant tectonic activity started in the Pamir.

In the Kekeya section which is also located in the southwestern edge of the Tarim basin, aeolian silt deposition started in the Artux Fm and the loess deposition continued through the Artux and Xiyu Fm (Tada et al., 2010) although there is little clear evidence of the loess deposition in the Aertashi section because of the continuous occurrence of the consistent river system. Based on this evidence, it is interpreted that the Tarim basin has been continuously under the arid condition at least since the deposition of the Artux Fm. (Zheng et al., 2010, 2015). Although the dry condition in the Tarim basin occurred in late Eocene, the timing of the onset of the loess deposition in the Kekeya section is much later at the boundary between stages 2 and 3 at ca. 26 Ma (Zheng et al., 2015), which indicates the possibility that the major tectonic event in the Pamir is associated with the intensification of the dry condition in the Tarim basin. Further research of the paleo-environment in the Tarim basin is necessary for more detailed discussion.

## Conclusions

The ESR signal intensity and the CI analyses and thin section observation were conducted for the fluvial sandstone from the Aertashi section on the southwest edge of the Tarim basin to examine the provenance changes in the drainage area of the paleo-Yarkand river. The result suggests the provenance of fluvial sediments at the Aertashi section at five times approximately at 34 Ma, 26 Ma, 20 Ma, 17 Ma, and 15 Ma. Based on this observation, we divided the sequence into 6 provenance stages. Thin section observation of fluvial sandstone shows the types of rocks exposed in drainage areas are dominantly sandstone, mudstone, limestone, and chert throughout the sequence, and the contribution of metamorphic rocks and volcanic rocks started to increase in stage 6. Significant change in the grain composition at the boundary between stage 5 and stage 6 at ca. 15 Ma suggests the expansion of the drainage area and acquisition of a new source rocks such as volcanic rocks and granitic plutonic rocks now exposing in the North Pamir terrane. From these results of this study and previous provenance study (Blayney et al., 2016), the major tectonic events in the NE Pamir was interpreted to occur at ca. 26 Ma, ca. 20 Ma, and ca. 15 Ma. On the other hand, the first appearance of the desert dunes was ca. 34 Ma in the Aertashi section (Zheng et al., 2010; Blayney et al., 2019) that precedes the major tectonic events in the NE Pamir revealed in this study. It is likely that the Tarim basin became the relatively arid condition before the major Cenozoic tectonic events in the NE Pamir and the arid condition might have intensified by the uplift of the NE Pamir around 26 Ma which is almost simultaneous to the initiation of loess deposition at the Kekeya section (Tada et al., 2010).

## Abbreviations

ESR: Electron Spin Resonance; CI: Crystallinity Index; KYTS: Kasugar-Yecheng Transfer System; Fm.: formation

# Declarations

## Availability of data and material

The datasets analysed during the current study are available from the corresponding author on reasonable request

## Competing interests

The authors declare that they have no competing interest.

## Funding

This work was jointly supported by National Natural Science Foundation of China (NSFC) (U1902208, 41991323 and 4188101) to the Strategic Priority Research Program of Chinese Academy of Sciences (XDB26020301), and the Second Tibetan Plateau Scientific Expedition and Research (2019QZKK0704) to Hongbo Zheng

## Authors' contributions

RT proposed the topic, conceived and designed the study. AS carried out the experiment, analyzed the data, and wrote the manuscript. TY, HS, NS, AK, KW, and HZ collaborated with the corresponding author in the construction of manuscript. All authors read and approved the final manuscript.

## Acknowledgements

We thank the staff at the Takasaki Advanced Radiation Research Institute, National Institute for Quantum and Radiological Science and Technology (QST) for the assistance with  $\gamma$ -ray irradiation.

# References

- Amidon, W.H., Hynek, S.A. (2010) Exhumational history of the north central Pamir. *Tectonics* 29, 1–13.  
<https://doi.org/10.1029/2009TC002589>
- An, Z., Kutzbach, J.E., Prell, W.L., Porter, S.C. (2001) Evolution of Asian monsoons and phased uplift of the Himalaya - Tibetan plateau since Late Miocene times. *Nature* 411, 62–66.  
<https://doi.org/10.1038/35075035>
- Bande, A., Sobel, E.R., Mikolaichuk, A., Acosta, V.T. (2015) Talas – Fergana Fault Cenozoic timing of deformation and its relation to Pamir indentation. *Geol. Soc. London, Spec. Publ.*  
<https://doi.org/10.1144/SP427.1>
- Bershaw, J., Garzzone, C.N., Schoenbohm, L., Gehrels, G., Tao, L. (2012) Cenozoic evolution of the Pamir plateau based on stratigraphy, zircon provenance, and stable isotopes of foreland basin sediments at

Oytag (Wuyitake) in the Tarim Basin (west China). *J. Asian Earth Sci.* 44, 136–148.

<https://doi.org/10.1016/j.jseaes.2011.04.020>

Blayney, T., Najman, Y., Dupont-Nivet, G., Carter, A., Millar, I., Garzanti, E., Sobel, E.R., Rittner, M., Andò, S., Guo, Z., Vezzoli, G. (2016) Indentation of the Pamirs with respect to the northern margin of Tibet: Constraints from the Tarim basin sedimentary record. *Tectonics* 35, 2345–2369.

<https://doi.org/10.1002/2016TC004222>.

Blayney, T., Dupont-Nivet, G., Najman, Y., Proust, J.N., Meijer, N., Roperch, P., Sobel, E.R., Millar, I., Guo, Z. (2019) Tectonic Evolution of the Pamir Recorded in the Western Tarim Basin (China): Sedimentologic and Magnetostratigraphic Analyses of the Aertashi Section. *Tectonics* 38, 492–515.

<https://doi.org/10.1029/2018TC005146>

Bosboom, R.E., Dupont-nivet, G., Houben, A.J.P., Brinkhuis, H., Villa, G., Mandic, O., Stoica, M., Zachariasse, W.J., Guo, Z., Li, C., Krijgsman, W. (2011) Late Eocene sea retreat from the Tarim Basin ( west China ) and concomitant Asian paleoenvironmental change. *Palaeogeogr. Palaeoclimatol. Palaeoecol.* 299, 385–398.

<https://doi.org/10.1016/j.palaeo.2010.11.019>

Bosboom, R., Dupont-Nivet, G., Grothe, A., Brinkhuis, H., Villa, G., Mandic, O., Stoica, M., Huang, W., Yang, W., Guo, Z., Krijgsman, W. (2014) Linking Tarim Basin sea retreat (west China) and Asian aridification in the late Eocene. *Basin Res.* 26, 621–640. <https://doi.org/10.1111/bre.12054>

Bosboom, R., Dupont-nivet, G., Grothe, A., Brinkhuis, H., Villa, G., Mandic, O., Stoica, M., Kouwenhoven, T., Huang, W., Yang, W., Guo, Z. (2014) Timing , cause and impact of the late Eocene stepwise sea retreat from the Tarim Basin ( west China ). *Palaeogeogr. Palaeoclimatol. Palaeoecol.* 403, 101–118.

<https://doi.org/10.1016/j.palaeo.2014.03.035>

Bougeois, L., Dupont-Nivet, G., de Rafélis, M., Tindall, J.C., Proust, J.-N., Reichart, G.-J., de Nooijer, L.J., Guo, Z., Ormukov, C. (2018) Asian monsoons and aridification response to Paleogene sea retreat and Neogene westerly shielding indicated by seasonality in Paratethys oysters. *Earth Planet. Sci. Lett.* 485, 99–110. <https://doi.org/10.1016/j.epsl.2017.12.036>

<https://doi.org/10.1016/j.epsl.2017.12.036>

Burtman, V.S., Molnar, P. (1993) Geological and geophysical evidence for deep subduction beneath the Pamir. *Spec. Pap. Geol. Soc. Am.* 281, 1–76. <https://doi.org/10.1130/SPE281-p1>

Cao, K., Xu, Y., Wang, G., Zhang, K., van der Beek, P., Wang, C., Jiang, S., Bershaw, J. (2014) Neogene Source-to-Sink Relations between the Pamir and Tarim Basin: Insights from Stratigraphy, Detrital Zircon Geochronology, and Whole-Rock Geochemistry. *J. Geol.* 122, 433–454. <https://doi.org/10.1086/676478>

Cao, K., Wang, G.C., Bernet, M., van der Beek, P., Zhang, K.X. (2015) Exhumation history of the West Kunlun Mountains, northwestern Tibet: Evidence for a long-lived, rejuvenated orogen. *Earth Planet. Sci. Lett.* 432, 391–403. <https://doi.org/10.1016/j.epsl.2015.10.033>

- Chapman, J.B., Carrapa, B., Ballato, P., DeCelles, P.G., Worthington, J., Oimahmadov, I., Gadoev, M., Ketcham, R. (2017) Intracontinental subduction beneath the Pamir Mountains: Constraints from thermokinematic modeling of shortening in the Tajik fold-and-thrust belt. *Bull. Geol. Soc. Am.* 129, 1450–1471. <https://doi.org/10.1130/B31730.1>
- Chen, X., Chen, H., Lin, X., Cheng, X., Yang, R., Ding, W., Gong, J., Wu, L., Zhang, F., Chen, S., Zhang, Y., Yan, J. (2018) Arcuate Pamir in the Paleogene? Insights from a review of stratigraphy and sedimentology of the basin fills in the foreland of NE Chinese Pamir, western Tarim Basin. *Earth-Science Rev.* 180, 1–16. <https://doi.org/10.1016/j.earscirev.2018.03.003>
- Clift, P.D., Zheng, H., Carter, A., Böning, P., Jonell, T.N., Schorr, H., Shan, X., Pahnke, K., Wei, X., Rittenour, T. (2017) Controls on erosion in the western Tarim Basin: Implications for the uplift of northwest Tibet and the Pamir. *Geosphere* 13, 1747–1765. <https://doi.org/10.1130/GES01378.1>
- Cowgill, E. (2010) Cenozoic right-slip faulting along the eastern margin of the Pamir salient, northwestern China. *GSA Bull.* 122, 145–161. <https://doi.org/10.1130/B26520.1>
- Decelles, P.G., Kapp, P., Gehrels, G.E., Ding, L. (2014) Paleocene-Eocene foreland basin evolution in the Himalaya of southern Tibet and Nepal: Implications for the age of initial India-Asia collision. *Tectonics* 33, 824–849. <https://doi.org/10.1002/2014TC003522>
- Dupont-Nivet, G., Krijgsman, W., Langereis, C.G., Abels, H.A., Dai, S., Fang, X. (2007) Tibetan plateau aridification linked to global cooling at the Eocene–Oligocene transition. *Nature* 445, 635–638. <https://doi.org/10.1038/nature05516>
- Feigl, F.J., Fowler, W.B., Yip, K.L. (1974) Oxygen vacancy model for the E1' center in SiO<sub>2</sub>. *Solid State Commun.* 14, 225–229. [https://doi.org/10.1016/0038-1098\(74\)90840-0](https://doi.org/10.1016/0038-1098(74)90840-0)
- Heermance, R. V, Pearson, J., Moe, A., Langtao, L., Jianhong, X., Jie, C., Richter, F., Garziona, C.N., Junsheng, N., Bogue, S. (2018) Erg deposition and development of the ancestral Taklimakan Desert (western China) between 12.2 and 7.0 Ma. *Geology* 46, 919–922. <https://doi.org/10.1130/G45085.1>
- Horn, C., Straathof, J., Abels, H.A., Xu, Y., Utescher, T., Dupont-Nivet, G. (2012) A late Eocene palynological record of climate change and Tibetan Plateau uplift (Xining Basin, China). *Palaeogeogr. Palaeoclimatol. Palaeoecol.* 344–345, 16–38. <https://doi.org/10.1016/j.palaeo.2012.05.011>
- Huang, C., Hinnov, L. (2019) Astronomically forced climate evolution in a saline lake record of the middle Eocene to Oligocene, Jiangnan Basin, China. *Earth Planet. Sci. Lett.* 528, 115846. <https://doi.org/10.1016/j.epsl.2019.115846>
- Isozaki, Y., Tada, R., Sun, Y., Zheng, H., Toyoda, S., Sugiura, N., Karasuda, A., Hasegawa, H. (2020). Origin of aeolian dust emitted from the Tarim Basin based on the ESR signal intensity and crystallinity index of

- quartz: The recycling system of fine detrital material within the basin. *Geological Magazine*, 157(5), 707-718. <https://doi.org/10.1017/S0016756820000242>
- Jiang, X.D., Li, Z.X. (2014) Seismic reflection data support episodic and simultaneous growth of the Tibetan Plateau since 25Myr. *Nat. Commun.* 5, 1–7. <https://doi.org/10.1038/ncomms6453>.
- Kaya, M.Y., Dupont-Nivet, G., Proust, J.N., Roperch, P., Bougeois, L., Meijer, N., Frieling, J., Fioroni, C., Özkan Altiner, S., Vardar, E., Barbolini, N., Stoica, M., Aminov, J., Mamtimin, M., Zhaojie, G. (2019) Paleogene evolution and demise of the proto-Paratethys Sea in Central Asia (Tarim and Tajik basins): Role of intensified tectonic activity at ca. 41 Ma. *Basin Res.* 461–486. <https://doi.org/10.1111/bre.12330>
- Klug, H. P. and Alexander L. E. 1974. "X-Ray Diffraction Procedure, 2<sup>nd</sup> ed., 966 pp., John Wiley, Hoboken, N. J
- Kutzbuch J. E., Prell, W. L., and Ruddiman, Wm. F. (1993) Sensitivity of Eurasian Climate to Surface Uplift of the Tibetan Plateau. *The Journal of Geology*, volume 101, 177-190. <https://doi.org/10.1086/648215>
- Li, X., Zhang, R., Zhang, Z., Yan, Q. (2018) What enhanced the aridity in Eocene Asian inland: Global cooling or early Tibetan Plateau uplift? *Palaeogeogr. Palaeoclimatol. Palaeoecol.* 510, 6–14. <https://doi.org/10.1016/j.palaeo.2017.10.029>
- Li, G., Sandiford, M., Fang, A., Kohn, B., Sandiford, D., Fu, B., Zhang, T., Cao, Y., Chen, F. (2019) Multi-stage exhumation history of the West Kunlun orogen and the amalgamation of the Tibetan Plateau. *Earth Planet. Sci. Lett.* 528, 115833. <https://doi.org/10.1016/j.epsl.2019.115833>
- Manabe, S., and A. J. Broccoli. (1990) Mountains and Arid Climates of Middle Latitudes. *Science* 247 (1969): 192–95. <https://doi.org/10.1126/science.247.4939.192>
- Murata, K., Norman, M.. (1976) An Index of Crystallinity for Quartz. *Am. J. Sci.* 276, 1120–1130. <https://doi.org/10.2475/ajs.276.9.1120>
- Najman, Y. (2006) The detrital record of orogenesis: A review of approaches and techniques used in the Himalayan sedimentary basins. *Earth-Science Reviews*, 74(1–2), 1–72. <https://doi.org/10.1016/j.earscirev.2005.04.004>
- National Center for Atmospheric Research Staff (Eds). Last modified 20 Sep 2018. "The Climate Data Guide: GPCC: Global Precipitation Climatology Centre."
- Ramstein, G., Fluteau, F., Besse, J., Joussaume, S. (1997) Effect of orogeny, plate motion and land-sea distribution on Eurasian climate change over the past 30 million years. *Nature* 386, 788–795. <https://doi.org/10.1038/386788a0>
- Robinson, A.C., Yin, A., Manning, C.E., Harrison, T.M., Zhang, S.H., Wang, X.F. (2007) Cenozoic evolution of the eastern Pamir: Implications for strain-accommodation mechanisms at the western end of the

Himalayan-Tibetan orogen. *Bull. Geol. Soc. Am.* 119, 882–896. <https://doi.org/10.1130/B25981.1>

Robinson, A.C., Ducea, M., Lapen, T.J. (2012) Detrital zircon and isotopic constraints on the crustal architecture and tectonic evolution of the northeastern Pamir. *Tectonics* 31, 1–16.

<https://doi.org/10.1029/2011TC003013>

Rutte, D., Ratschbacher, L., Khan, J., Stübner, K., Hacker, B.R., Stearns, M.A., Enkelmann, E., Jonckheere, R., PfänderGulzar, J.A., Sperner, B., Tichomirowa, M. (2017) Building the Pamir-Tibetan Plateau—Crustal stacking, extensional collapse, and lateral extrusion in the Central Pamir: 2. Timing and rates. *Tectonics* 36, 342–384. <https://doi.org/10.1002/2016TC004293>

Smit, M.A., Ratschbacher, L., Kooijman, E., Stearns, M.A. (2014) Early evolution of the Pamir deep crust from Lu-Hf and U-Pb geochronology and garnet thermometry. *Geology* 42, 1047–1050.

<https://doi.org/10.1130/G35878.1>

Sobel, E.R., Dumitru, T. A. (1997) Thrusting and exhumation around the margins of the western Tarim basin during the India-Asia collision. *J. Geophys. Res. Solid Earth* 102, 5043–5063.

<https://doi.org/10.1029/96JB03267>

Sobel, E.R., Chen, J., Schoenbohm, L.M., Thiede, R., Stockli, D.F., Sudo, M., Strecker, M.R. (2013) Oceanic-style subduction controls late Cenozoic deformation of the Northern Pamir orogen. *Earth Planet. Sci. Lett.* 363, 204–218. <https://doi.org/10.1016/j.epsl.2012.12.009>

Stearns, M.A., Hacker, B.R., Ratschbacher, L., Rutte, D., Kylander-Clark, A.R.C. (2015) Titanite petrochronology of the Pamir gneiss domes: Implications for middle to deep crust exhumation and titanite closure to Pb and Zr diffusion. *Tectonics* 34, 784–802. <https://doi.org/10.1002/2014TC003774>

Sun, D., Bloemendal, J., Rea, D.K., Vandenberghe, J., Jiang, F., An, Z., Su, R. (2002) Grain-size distribution function of polymodal sediments in hydraulic and aeolian environments, and numerical partitioning of the sedimentary components. *Sediment. Geol.* [https://doi.org/10.1016/S0037-0738\(02\)00082-9](https://doi.org/10.1016/S0037-0738(02)00082-9)

Sun, D., Bloemendal, J., Yi, Z., Zhu, Y., Wang, X., Zhang, Yuebao, Li, Z., Wang, F., Han, F., Zhang, Yan (2011) Palaeomagnetic and palaeoenvironmental study of two parallel sections of late Cenozoic strata in the central Taklimakan Desert: Implications for the desertification of the Tarim Basin. *Palaeogeogr. Palaeoclimatol. Palaeoecol.* 300, 1–10. <https://doi.org/10.1016/j.palaeo.2010.11.015>

Sun, H., Liu, X. (2018) Impacts of the uplift of four mountain ranges on the arid climate and dust cycle of inland Asia. *Palaeogeogr. Palaeoclimatol. Palaeoecol.* 505, 167–179.

<https://doi.org/10.1016/j.palaeo.2018.05.040>

Sun, J., Zhang, Z., Zhang, L. (2009) New evidence on the age of the Taklimakan Desert. *Geology* 37, 159–162. <https://doi.org/10.1130/G25338A.1>

- Sun, J., Windley, B.F. (2015) Onset of aridification by 34 Ma across the Eocene-Oligocene transition in Central Asia. *Geology* 43, 1015–1018. <https://doi.org/10.1130/G37165.1>
- Sun, J., Liu, W., Liu, Z., Deng, T., Windley, B.F., Fu, B. (2017) Extreme aridification since the beginning of the Pliocene in the Tarim Basin, western China. *Palaeogeogr. Palaeoclimatol. Palaeoecol.* 485, 189–200. <https://doi.org/10.1016/j.palaeo.2017.06.012>
- Tada, R., Sato, S., Irino, T., Matsui, H., Kennett, J.P. (2000) 25 . MILLENNIAL-SCALE COMPOSITIONAL VARIATIONS IN LATE QUATERNARY SEDIMENTS AT SITE 1017 , SOUTHERN CALIFORNIA 1. *Proc. Ocean Drill. Program, Sci. Results* 167. <http://doi.org/10.2973/odp.proc.sr.167.222.2000>
- Tada, R., Zheng, H., Sugiura, N., Isozaki, Y., Hasegawa, H., Sun, Y., Yang, W., Wang, K., Toyoda, S. (2010) Desertification and Dust Emission History of the Tarim Basin and Its Relation to the Uplift of Northern Tibet. *Geol. Soc. London, Spec. Publ.* 342, 45–65. <https://doi.org/10.1144/SP342.5>
- Toyoda, S. (1992) Production and Decay Characteristics of Paramagnetic Defects in Quartz: Applications to ESR Dating, Osaka University, Japan, Ph. D Thesis
- Toyoda, S., Hattori, W. (2000) Formation and decay of the E 1 ' center and of its precursor. *Appl. Radiat. Isot.* 52, 1351–1356. <https://doi.org/10.1016/j.apradiso.2004.08.014>
- Toyoda, S., Naruse, T. (2002) Eolian Dust from the Asian Deserts to the Japanese Islands since the Last Glacial Maximum: the Basis for the ESR Method. *Transactions* 23, 811–820.
- Uno, I., Eguchi, K., Yumimoto, K., Takemura, T., Shimizu, A., Uematsu, M., Liu, Z., Wang, Z., Hara, Y., Sugimoto, N. (2009) Asian dust transported one full circuit around the globe. *Nat. Geosci.* 2, 557–560. <https://doi.org/10.1038/ngeo583>
- Wei, X., Zheng, H., Wang, P., Tada, R., Clift, P.D., Jourdan, F., Luo, C., Chen, H. (2018) Miocene Volcaniclastic Sequence Within the Xiyu Formation from Source to Sink: Implications for Drainage Development and Tectonic Evolution in Eastern Pamir, NW Tibetan Plateau. *Tectonics*. <https://doi.org/10.1029/2018TC005008>
- Yin, A., Rumelhart, P.E., Butler, R., Cowgill, E., Harrison, T.M., Foster, D.A., Ingersoll, R. V., Zhang, Q., Zhou, X.Q., Wang, X.F., Hanson, A., Raza, A. (2002) Tectonic history of the Altyn Tagh fault system in northern Tibet inferred from Cenozoic sedimentation. *Bull. Geol. Soc. Am.* 114, 1257–1295. [https://doi.org/10.1130/0016-7606\(2002\)114<1257:THOTAT>2.0.CO;2](https://doi.org/10.1130/0016-7606(2002)114<1257:THOTAT>2.0.CO;2)
- Zheng, H., Huang, X., Butcher, K. (2006) Lithostratigraphy, petrography and facies analysis of the Late Cenozoic sediments in the foreland basin of the West Kunlun. *Palaeogeogr. Palaeoclimatol. Palaeoecol.* 241, 61–78. <https://doi.org/10.1016/j.palaeo.2006.06.015>
- Zheng, H., Tada, R., Jia, J., Lawrence, C., Wang, K. (2010) Cenozoic sediments in the southern Tarim Basin: implications for the uplift of northern Tibet and evolution of the Taklimakan Desert. *Geol. Soc.*

London, Spec. Publ. 342, 67–78. <https://doi.org/10.1144/SP342.6>

Zheng, H., Wei, X., Tada, R., Clift, P.D., Wang, B., Jourdan, F., Wang, P., He, M. (2015) Late Oligocene–early Miocene birth of the Taklimakan Desert. *Proc. Natl. Acad. Sci.* 112, E5558–E5559. <https://doi.org/10.1073/pnas.1517735112>

## Figures

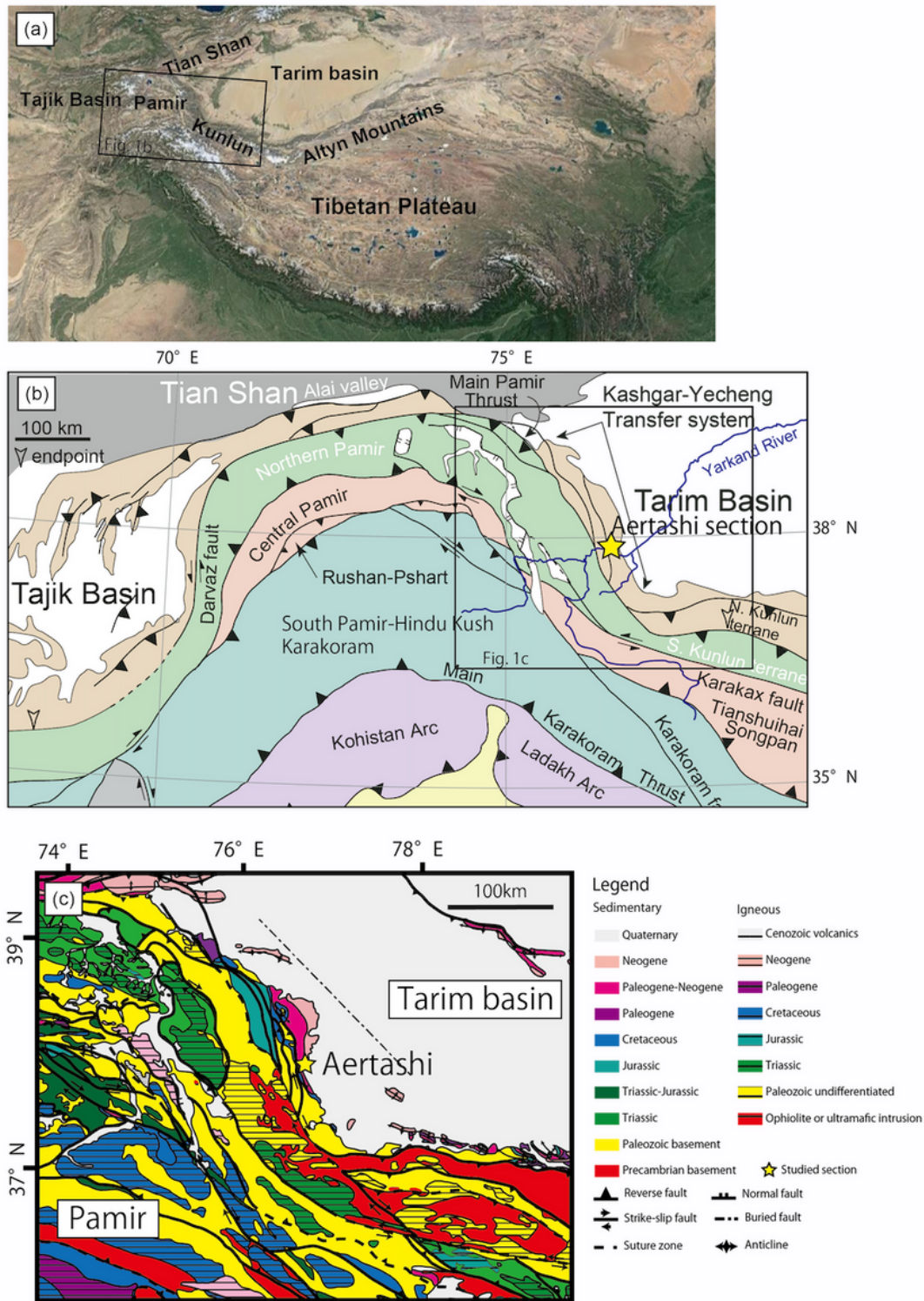


**Figure 1**

Tectonic settings in this study. (a) Location of the Pamir (Google Map). (b) Simplified tectonic settings of the Tarim basin and surrounding areas (modified after Cowgill, 2010). (c) Geological map of the eastern Pamir after Cao et al. (2015)

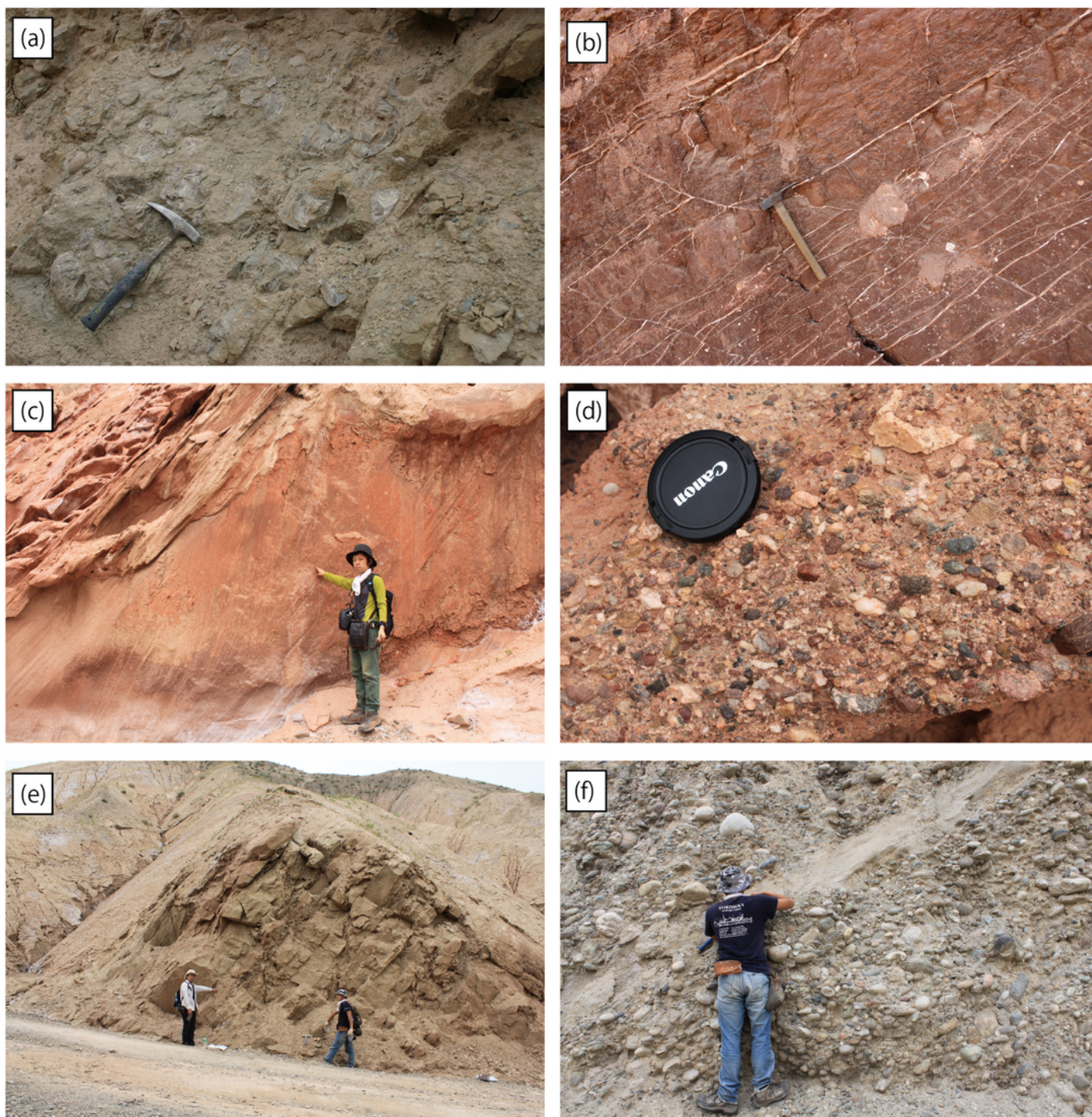


**Figure 2**

Photographs showing the typical lithology of each formation. (a) Green mudstone with shell fossils of the Wulagen Formation. (b) Reddish brown mudstone containing gypsum veins of the Bashibulake Formation. (c) Aeolian sandstone showing high-angle cross bedding of the bottom of the Wuqia Group. (d) Conglomerate of the lower part of the Artux Formation. (e) Alteration of orange and yellow fine

sandstone of the upper part of the Artux Formation. (f) Thick conglomerate and intercalated light yellowish gray fine sandstone of the Xiyu Formation.

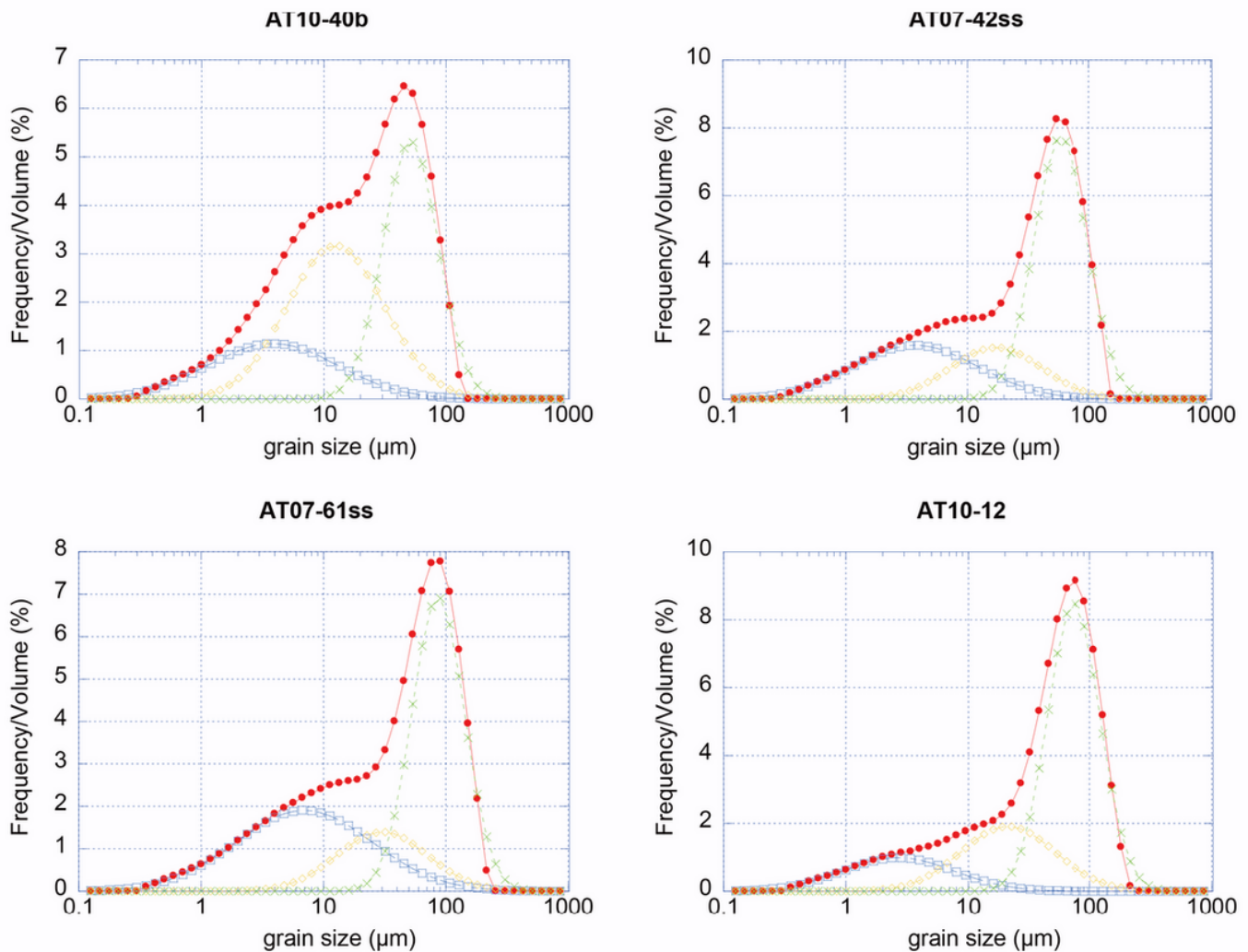


**Figure 3**

Typical grain size distributions of representative samples. Red shows measurement data. All samples from the Aertashi sections are composed of three sub-components and sub-population are shown with blue, yellow, and green lines. The 64-500 μm fraction used for the ESR and CI analyses in this study corresponds to the coarsest sub-population.

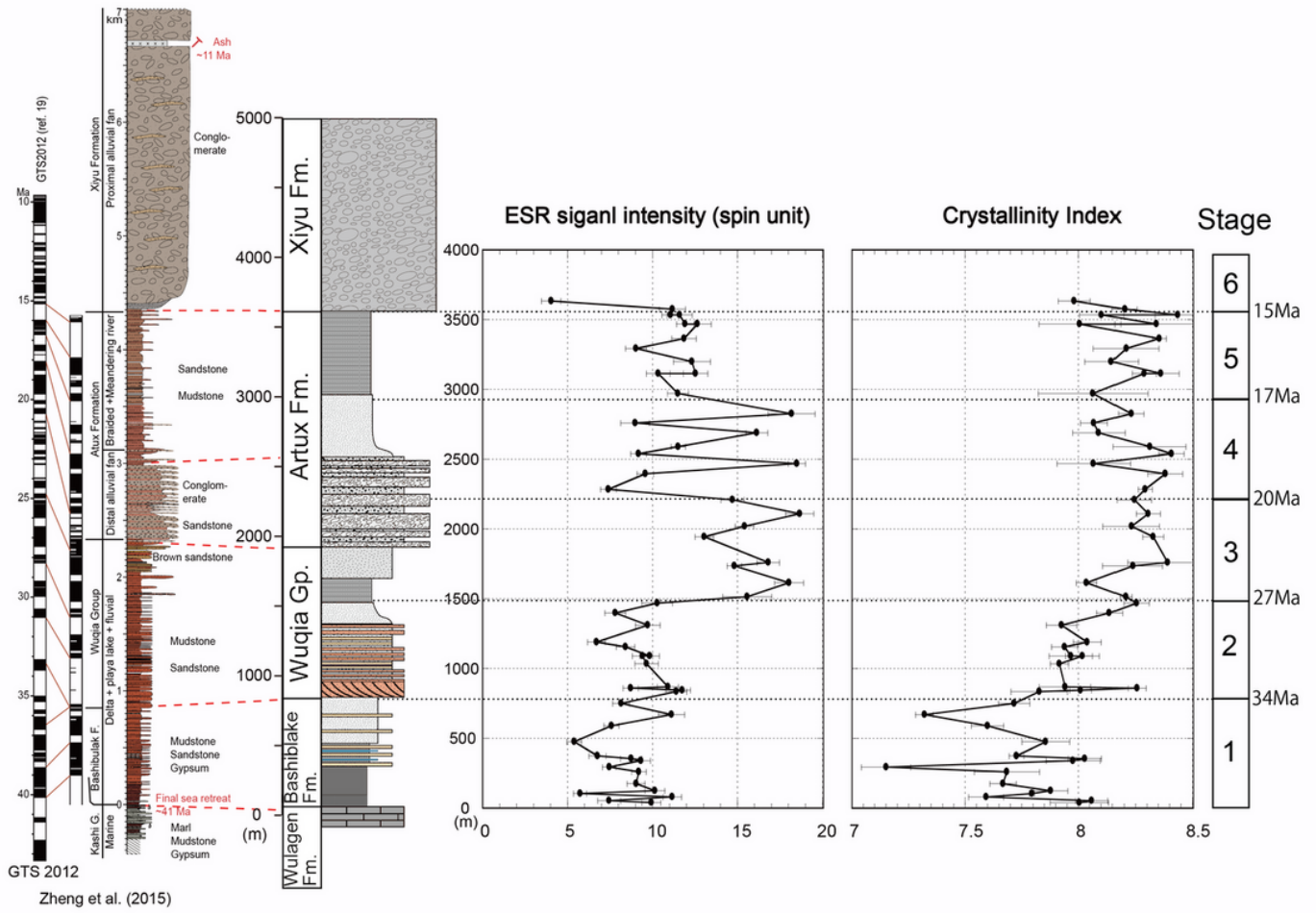


**Figure 4**

Temporal changes in the ESR signal intensity and the CI of the Aertashi section.

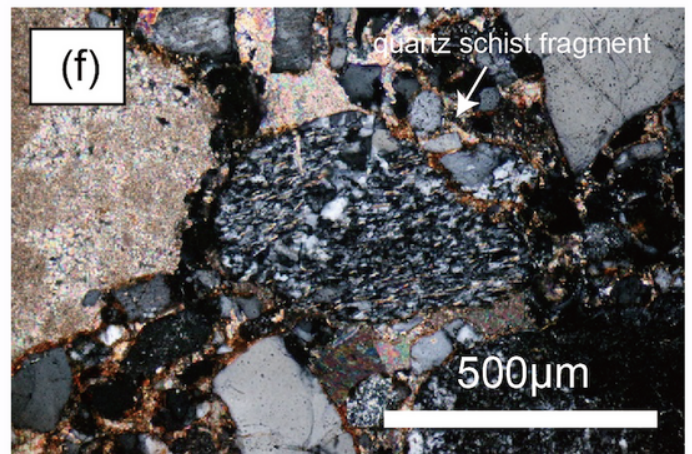
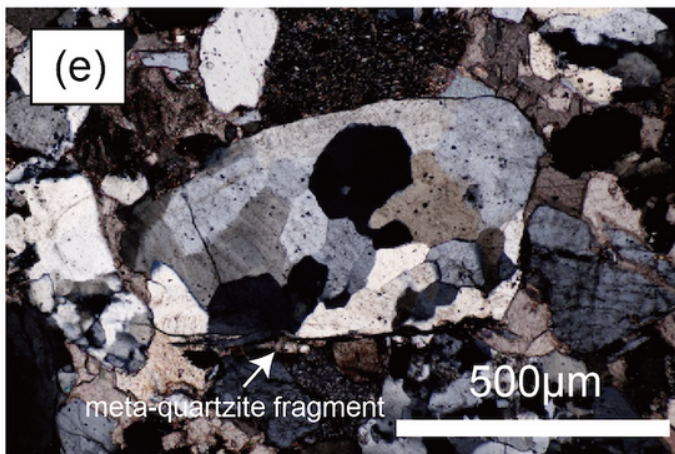
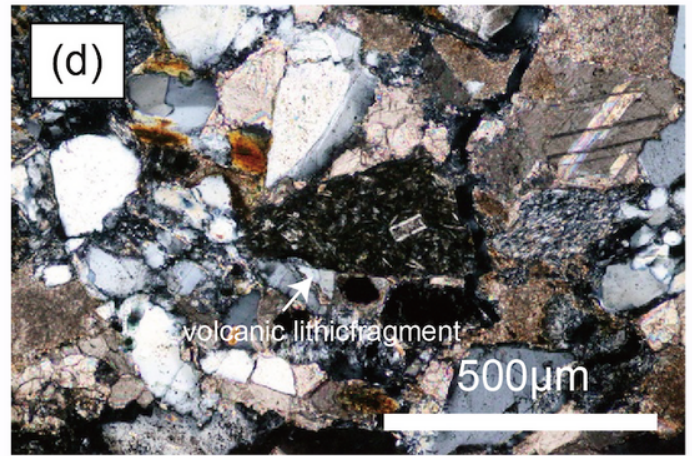
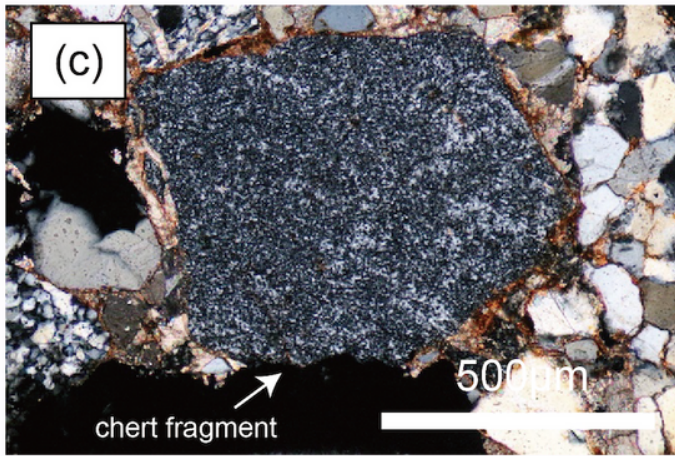
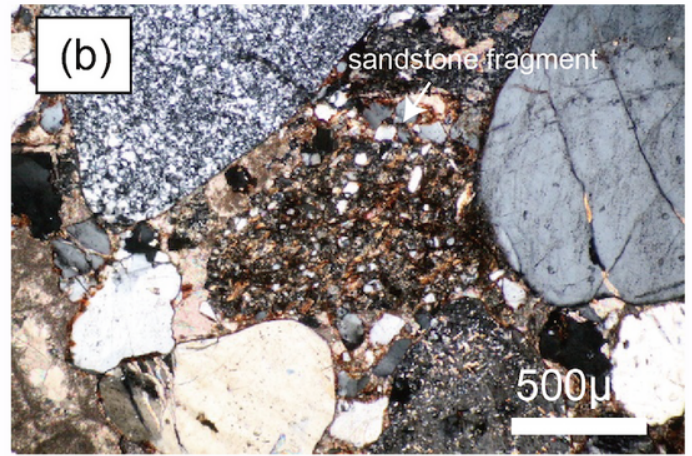
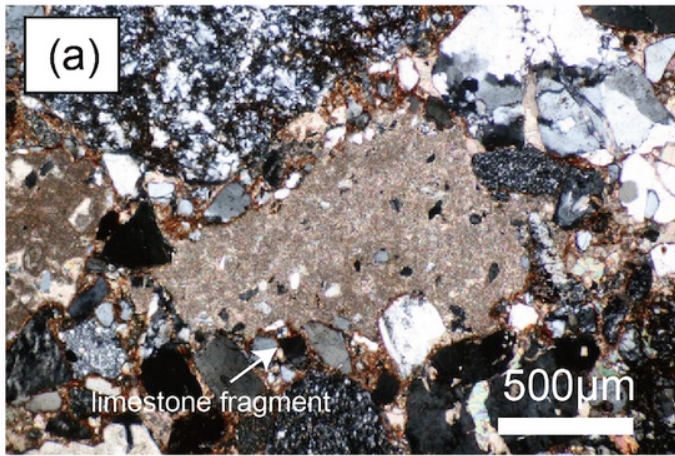


**Figure 5**

Photos of various types of lithic fragments in the Aertashi section. (a) Micritic limestone fragment. (b) Sandstone fragment. (c) Chert fragment. (d) Volcanic rock fragment. (e) Meta-quartzite fragment. (f) Quartz schist fragment.

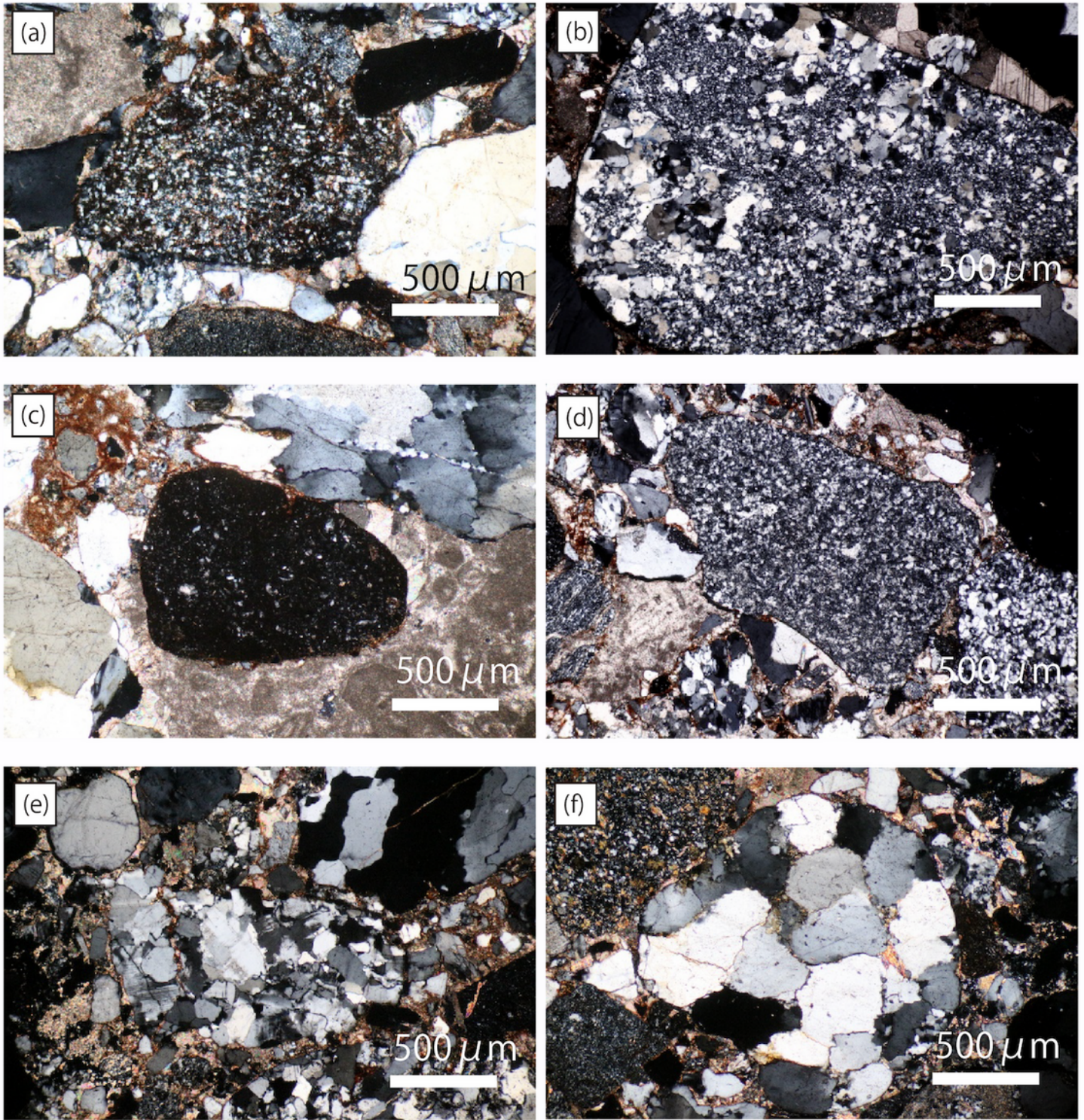


**Figure 6**

Photos of clastic rock fragments in the Aertashi section. (a) siltstone fragment. (b) Siliceous siltstone fragment. (c) Claystone fragment. (d) Siliceous claystone fragment. (e) Quartzo-feldspathic sandstone fragment. (f) Orthoquartzite fragment.

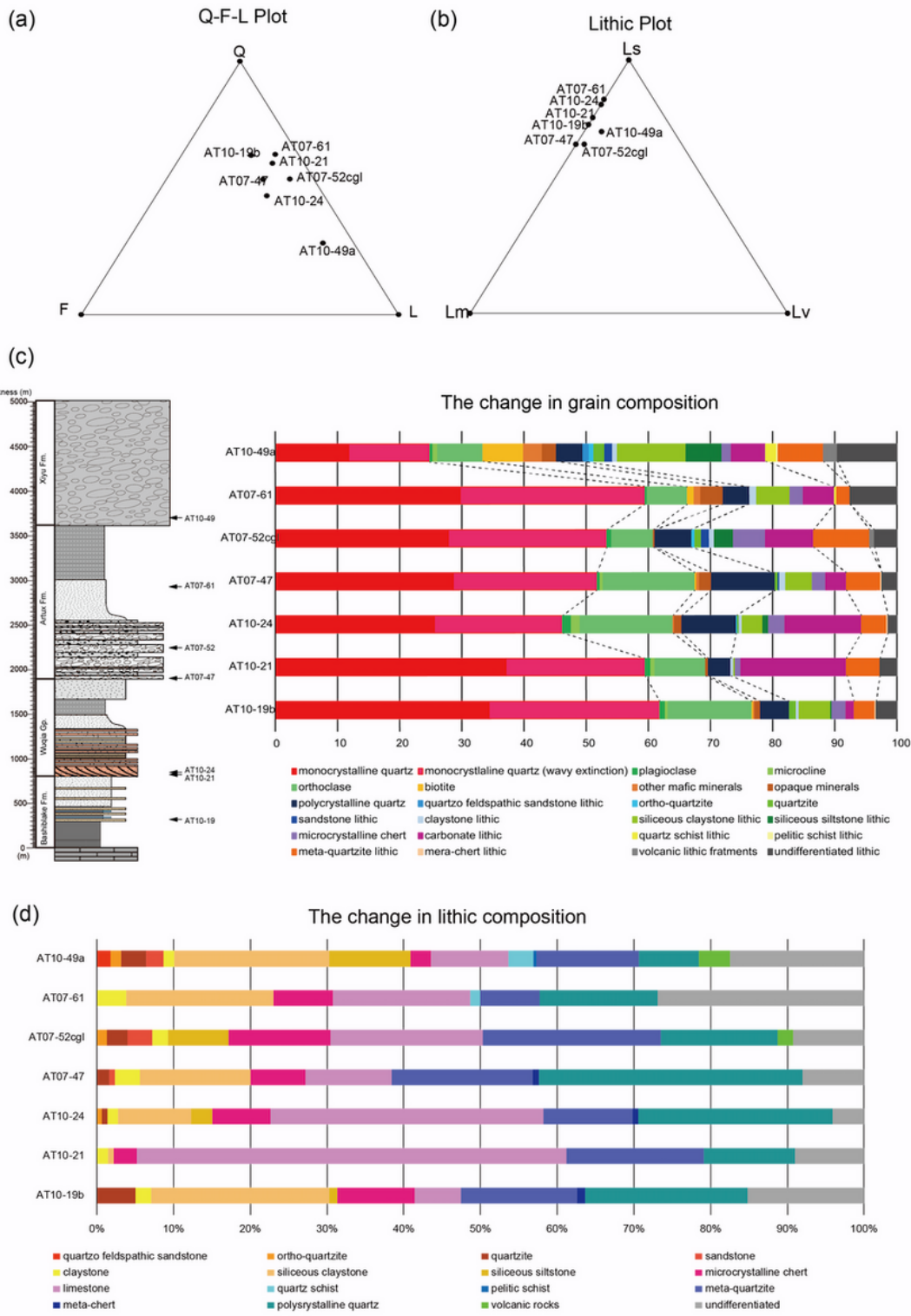


**Figure 7**

Changes in grain composition. (a) Quartz-Feldspar-Lithic plot. (b) Lithic plot showing the ratio of sedimentary rocks, volcanic rocks, and metamorphic rocks. (c) Changes in grain compositions of fluvial sandstone in the Aertashi section. (d) Changes in lithic fragments in the Aertashi section.

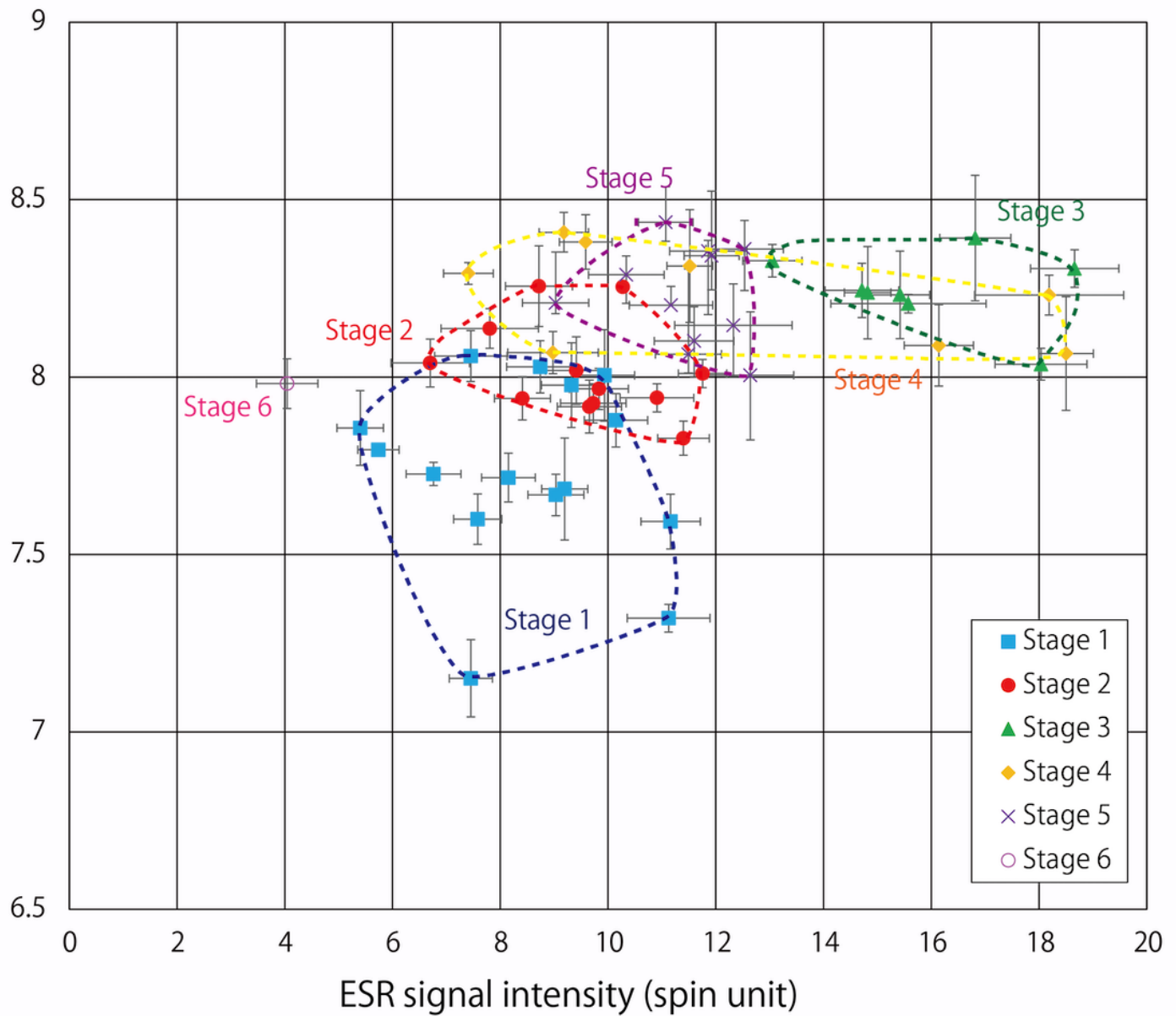


**Figure 8**

The ESR vs the CI plot. The relationship between the ESR signal intensity and Crystallinity Index (CI) of quartz in fine sand fraction of fluvial sandstone in the Aertashi section.

## Supplementary Files

This is a list of supplementary files associated with this preprint. Click to download.

- [Graphicalabstract.png](#)
- [supplementarytable1.xls](#)

- [supplementarytable2.xlsx](#)